

Novel design of interdigitated electrodes for piezoelectric transducers

Ahmed Jemai¹ and Fehmi Najar^{*1,2}

¹Applied Mechanics and Systems Research Laboratory, Tunisia Polytechnic School, BP 743, La Marsa 2078, University of Carthage, Tunisia

²IPEIEM, B.P 244, Tunis 2092, University of Tunis El Manar, Tunisia

(Received July 12, 2018, Revised July 22, 2018, Accepted September 11, 2018)

Abstract. Novel design of interdigitated electrodes capable of increasing the performance of piezoelectric transducers are proposed. The new electrodes' geometry improve the electromechanical coupling by offering an enhanced adaptation of the electric field to the interdigitated electrode configuration. The proposed analysis is based on finite element modeling and takes into account local polarization effect. It is shown that the proposed electrodes considerably increase the strain generation compared to flat electrode arrangement used for Macro Fiber Composite (MFC) and Active Fiber Composite (AFC) actuators. Also, electric field singularities are reduced allowing better reliability of the transducer against electric failure.

Keywords: interdigitated electrodes; piezoelectricity; sensor and actuator; polarization; piezocomposite

1. Introduction

Piezoelectric devices are extensively used for adaptive or smart structure applications. Both actuation, sensing and energy harvesting devices have been explored in aerospace, aeronautic, industrial, and automotive applications. Active wings (Prakash *et al.* 2016), active damping of aircraft panels (Inman *et al.* 2001, Sahu *et al.* 2015), and adaptive satellite antenna (Paradies *et al.* 1996), energy harvester (Avsar and Sahin 2016) and windmills (Jamal *et al.* 2015) are examples of such advances in these research areas.

The use of piezoelectricity for sensing and actuation is generally strongly related to the technology used to locate the active material between the electrodes that ensure energy transduction. The position of the electrodes along with the initial polarization of the material can activate different piezoelectric modes, for example the transverse d_{31} or the longitudinal d_{33} modes. In general, and because of its simplicity, parallel electrode configuration is used with different piezoelectric material, which allows the activation of the d_{31} mode if bending deformation is sought. However, it is known that the longitudinal mode coefficient d_{33} can be more than twice large as d_{31} . In order to take benefit from the longitudinal mode in bending deformation, interdigitated electrodes (IDEs) with flat surface electrodes has been introduced by Hagood *et al.* (1993).

Using Finite Element (FE) analysis, Bowen *et al.* (1999) showed that IDEs generates higher strain when compared to classical parallel electrodes for a given electric field. In addition, Zhang *et al.* (2016, 2015) studied MFC using the longitudinal d_{33} mode with arbitrary fiber orientation, by

using the FE method. They demonstrated that MFC- d_{33} device can produce larger actuation stress when the fiber reinforcement angle is properly chosen. The use of the FE method is suitable in this case because the electric field is no longer parallel to be approximated by simple analytical expression. If the material structure is periodic, such as MFC (Trindade and Benjeddou 2011, Zhang *et al.* 2017, Li *et al.* 2016) and AFC (Jemai *et al.* 2014) piezocomposite, a representative volume element can be used to reduce the computational time.

For microscale devices piezoelectricity has been used for actuation, sensing and also energy harvesting especially with IDE (Hong *et al.* 2006). Particularly, atomic force microscope probes are actuated using a piezoelectric layer (Moore and Kong 2017). Review of piezoelectric microsensors such as accelerometers, gyroscopes, pyroelectric detector, etc., can be found in (Tadigadapa and Mateti 2009, Muralt 2008). Microscale energy harvester are implemented with Micro-Electro-Mechanical Systems (MEMS) technology using cantilever beam structure with tip mass to reduce the fundamental frequency of the device (Lu *et al.* 2004, Ammar *et al.* 2005). In fact, the use of IDE in MEMS devices is restricted by the fact that classical microfabrication technology only allows one side deposition of the IDEs over the piezoelectric polycrystalline material (Muralt 2008). Nevertheless, the question of optimal electrode patterns is an open issue when the devices are built at the microscale level.

Despite the use of the d_{33} mode with IDEs and especially for energy harvesting application, the electrical energy generated from these devices can be low compared to conventional parallel electrodes devices (Sodano *et al.* 2006). This is due to reduced effective capacitance of the electrode configuration. Jemai *et al.* (2014, 2016) demonstrated that the electrical power is approximately the same when similar amount of active material is used. Also,

*Corresponding author, Ph.D.
E-mail: fehmi.najar@ept.rnu.tn

they showed that an optimization of electrode pattern and geometric dimensions, such as the number of electrode and both thickness and length layer, can drastically increase the performance of the energy harvester with IDEs, if they are accordingly chosen. In the same way, Kim *et al.* (2013) proved that the electrical power of the harvester with appropriate IDE design could exceed that of the conventional harvester.

In this work, it is proposed to design and analyze the performances of novel IDE shapes for piezoelectric actuators and compare them with the classical flat IDEs. Using the FE Method, the effect of the cross-section shape of the electrode on the performance and the electric field concentration is investigated by using two different numerical models; A classical model, in which the piezoelectric material is fully poled in the longitudinal direction only, and an advanced model that takes into account the electric field disturbance such as the variation of the poling direction near the electrodes. A comparison between two models is, then, given in order to appreciate the influence of the local geometric details on the performance of the various proposed IDEs.

2. Finite element modeling of the IDEs

The system examined, shown schematically in Fig. 1 is a beam of variable cross section, carrying a so called heavy tip mass M . Its mass moment of inertia with respect to the perpendicular axis at the centroid S is denoted by J_S . The publications (Abolghasemi and Jalali 2003, Younesian and Esmailzadeh 2010, Arvin and Bakhtiari-Nejad 2011) are considered also with rotating beams in which nonlinear oscillations are investigated. Analytical and experimental investigations on vibrating frames carrying concentrated masses with characteristics of frames have been studied by using analytical solutions and the finite element method A piezoelectric cantilever beam (Fig. 1(a)) is considered in this work. It is made of PZT-5A material, actuated by a constant voltage over Interdigitated Electrodes (IDEs).

A Finite Element (FE) model is developed using the commercial package ANSYS. It is used to compare the performances of different newly proposed electrodes. The IDEs have various cross-section designs that allow different electrical polarization distributions over the piezoelectric material (Fig. 1(b)). A coupled-field analysis is undertaken to correctly model the interactions between the electrical and mechanical domains.

For the proposed FE model, thanks to the aspect ratio of the beam, the edge and surface effects can be ignored. As a result, the electric field distribution does not vary along the z -direction and the FE models can be reduced to a 2D models (Fig. 1). In addition, since the IDEs describe a periodic pattern, the piezoelectric beam can be decomposed into a set of repeating unit cells where identical behavior can be observed. These cells are known as Representative Volume Element (RVE) (Fig. 1(b)).

As mentioned above, different shapes of the IDEs are proposed. These shapes could be directly etched into the piezoelectric material using microfabrication MEMS

techniques (Ghodssi and Lin 2011). Since both isotropic and anisotropic etching are available, it is proposed here, along with the classical surface deposited electrodes, two new electrode shapes with circular and triangular geometries. FE models of the RVEs with different cross-sections of the electrode are highlighted in Fig. 2.

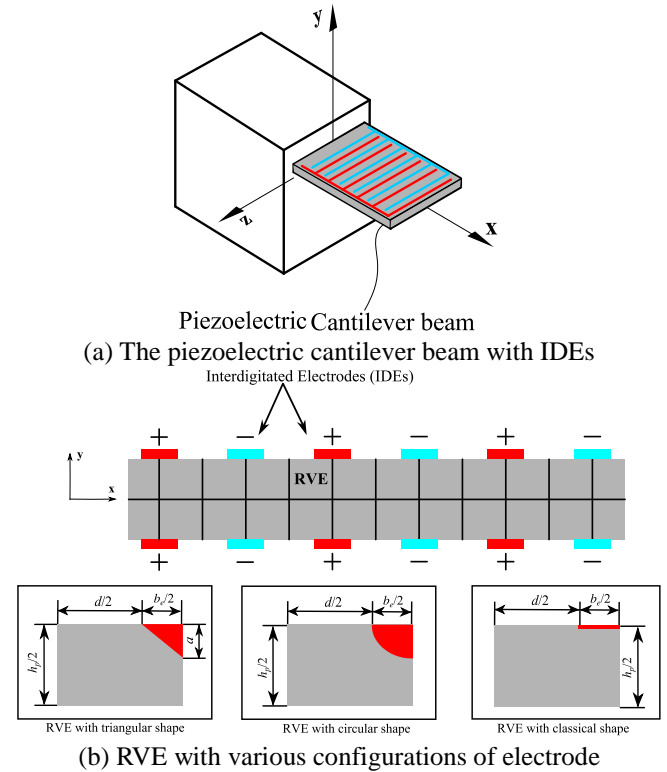


Fig. 1 Piezoelectric cantilever beam with IDEs and its RVE

Table 1 Material property for polarized and non-polarized PZT-5A

Material properties	Polarized PZT-5A	Non-Polarized PZT-5A	
Density ρ (kg/m ³)	7500	7500	
Elastic stiffness at constant electric field	C_{11}^E (GPa)	120	88
	C_{12}^E (GPa)	75.2	37.7
	C_{13}^E (GPa)	75.1	37.7
	C_{33}^E (GPa)	111	88
	C_{44}^E (GPa)	21.0	25.1
	C_{66}^E (GPa)	22.4	25.1
Piezoelectric constants	e_{13} (GPa)	-5.2	-
	e_{33} (GPa)	15.8	-
	e_{15} (GPa)	12.3	-
Permittivity at constant stress	$\epsilon_{11}^T / \epsilon_0$	1730	1000
	$\epsilon_{33}^T / \epsilon_0$	1700	1000

Table 2 Material properties for the electrodes

Young's modulus E_e (GPa)	Poisson's ration ν_e	Relative Permittivity
90	0.30	4.25

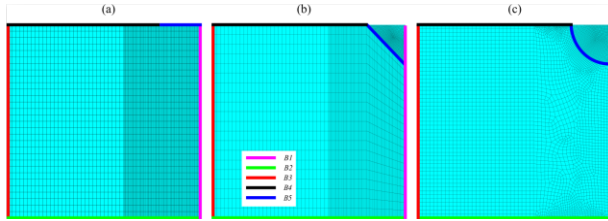


Fig. 2 Proposed FE meshing model of the RVEs with associated boundary conditions

The proposed active material is the monolithic piezoelectric PZT-5A whose properties are given in Table 1. The electrodes are made of 80% of Copper and 20% of Epoxy while the material properties used in the FE simulation are obtained using a rule of mixture and of the electrode are highlighted in Fig. 2.

The proposed active material is the monolithic piezoelectric PZT-5A whose properties are given in Table 1. The electrodes are made of 80% of Copper and 20% of Epoxy while the material properties used in the FE simulation are obtained using a rule of mixture and shown in Table 2. PLANE223 coupled-field elements are used to model the piezoelectric and electrode materials in the FE model.

To activate the piezoelectric material in the FE model, an electrical potential is applied directly on nodes located at the interface between electrode and piezoelectric material corresponding to the boundary B5 in Fig. 2. On the other hand, appropriate mechanical and electrical boundary conditions are imposed to the RVE by taking into account its periodic repeatability over longitudinal direction of the cantilever beam. A summary of these boundary conditions is shown in Table 3 where D is the electric displacement, V is the voltage applied to the positive electrodes, and U is the nodal displacement. It is also worth noting here that plane strain conditions are enforced in this analysis as recommended by Bowen *et al.* (Bowen *et al.* 2006). Also, the element mesh-size is adapted to the expected large variation of the electric field, therefore fine meshing is adopted underneath and near the electrodes.

For comparison purposes, two different FE models are considered. The first one, known here as the Classical Finite Element Model (CFEM), uses a fully poled piezoelectric material in the x-direction. This assumption is exclusively adequate for large electrode separations where polarization does not changes with the applied voltage (Bowen *et al.* 2006). The second FE model accounts for local variations of the poling direction due to curved electric field lines resulting from complex electrode pattern, it is known here as the Advanced Finite Element Model (AFEM).

Table 3 Boundary conditions for the displacement, electrical potential and electrical displacement applied to the RVE

Boundary number	Displacement	Electrical conditions
B1	Symmetry ($U_x = 0$)	$D_x = 0$
B2	Symmetry ($U_y = 0$)	$D_y = 0$
B3	U_x coupled	$V = 0$
B4	Free	$D_y = 0$
B5	Free	$V / 2 = 0.5kV$

Two steps technique are used to simulate the poling process simulation in the AFEM (Beckert and Kreher 2003, Paradies and Melnykowycz 2010). In the first step, the electric field lines are computed with non-polarized material, where the poling vectors are aligned with the x-axis for all elements. In the second step, the poling direction in each element is aligned with the electric field directions. So that, the updated configuration in each element is implemented by rotating the local coordinate system according to the polarization direction within that element. Moreover, the material becomes partially (or fully) poled depending on the intensity of the electric field on that element. Figs. 3(a)-3(c) show the local coordinate system within each element and the electric field distributions at the beginning and the end of the poling simulation process of the RVEs with classical (Cl), Triangular (Tr) and circular (Cr) electrodes, respectively.

The new simulated poling direction in each element should also be considered in the calculation of local changes of material's properties. The following poling strength factor XP is used to determine the poling state in an element

$$X_p = \begin{cases} 0 & \text{if } |E| < E_c \\ \frac{|E| - E_c}{E_s - E_c} & \text{if } E_c < |E| < E_s \\ 1 & \text{if } |E| > E_s \end{cases} \quad (1)$$

where $|E|$ is the absolute value of the total magnitude of the electric field given by $|E| = \sqrt{E_1^2 + E_2^2}$, where E_1 and E_2 are the electric fields in the x and y directions, respectively. Also, $E_c = 0.8 \times 10^6 \text{ V/m}$ and $E_s = 1.6 \times 10^6 \text{ V/m}$ are the coercive and saturated electric field values, respectively Nguyen *et al.* (2011). Therefore, local properties of the piezoelectric material are defined as follows

$$\begin{aligned} C_{ij}^E &= (C_{ij}^{E,P} - C_{ij}^{E,UP})X_p + C_{ij}^{E,UP} \\ \epsilon_{ij}^T &= (\epsilon_{ij}^{T,P} - \epsilon_{ij}^{T,UP})X_p + \epsilon_{ij}^{T,UP} \\ e_{ij} &= X_p e_{ij}^P \end{aligned} \quad (2)$$

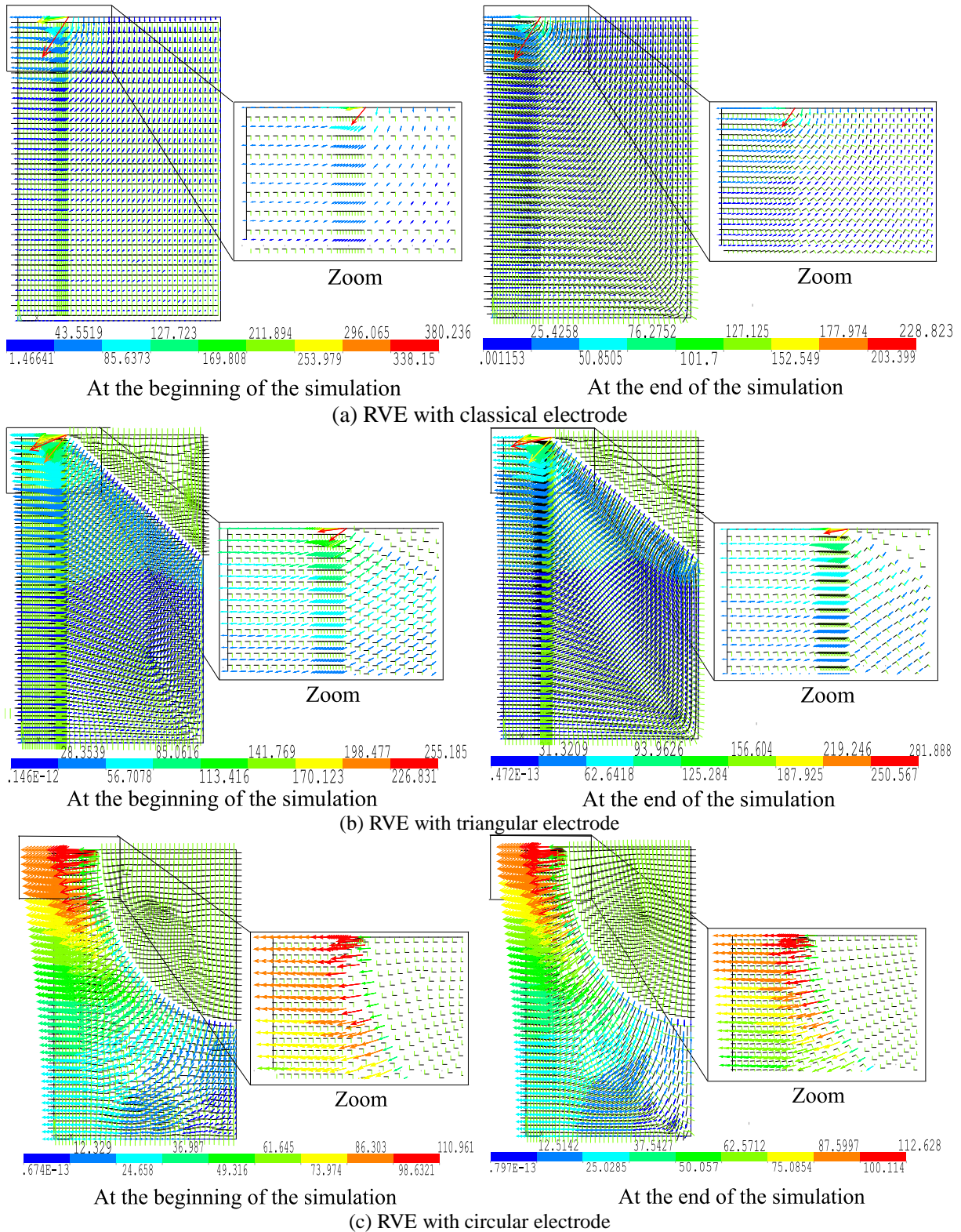


Fig. 3 Material orientation (triad) and electric field orientation at the beginning and the end of the poling simulation process of RVE

where the superscript P and UP designate respectively poled and unpoled states. If the local electric field is lower than the coercive field value, the material remains at its unpoled state. However, if the local electric field is higher

than the coercive field value, the material becomes partially poled and when it reaches the saturation field value, it becomes fully poled.

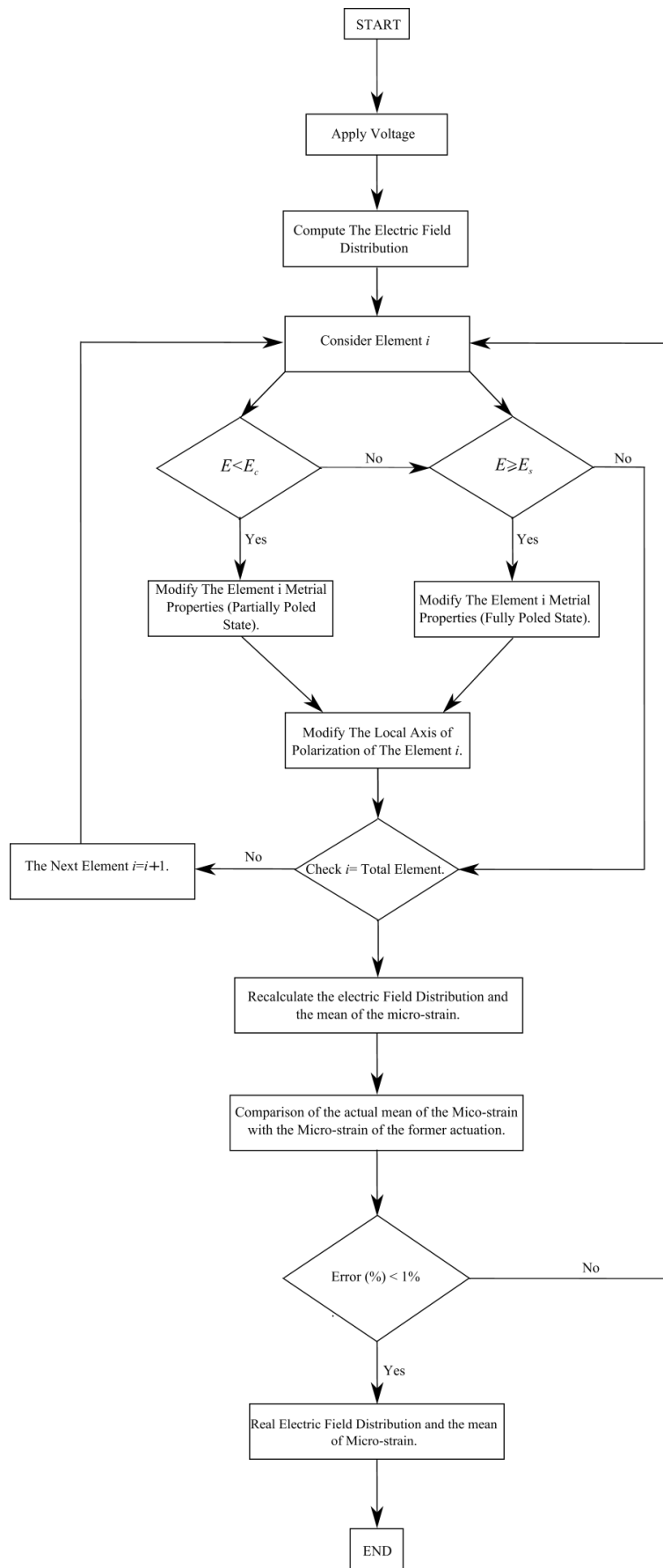


Fig. 4 Flow-chart for the proposed algorithm for electric field evaluation in the RVEs

Table 4 Convergence results of the micro-generated strain ($d/2 = 30\mu\text{m}$, $a = b_e/2 = 20\mu\text{m}$, $h_p/2 = 50\mu\text{m}$)

IDEs cross-section	1st Iteration	2nd Iteration	3rd Iteration	4th Iteration
Cl (Error)	1.890	1.930 (2.11%)	1.917 (0.67%)	1.922 (0.26%)
Tr (Error)	2.627	2.597 (1.14%)	2.607 (0.38%)	2.604 (0.11%)
Cr (Error)	3.907	3.839 (1.74%)	3.853 (0.36%)	3.851 (0.05%)

By changing the local material's properties and the poling direction in all elements, the electric field distribution and the generated strain are updated with the same geometry and boundary conditions. This procedure is iterated while the strain generation average is calculated at each step until the relative variation error of the strain is less than 1%, it is defined by

$$\text{Error (\%)} = \left| \frac{S_x^{(i)} - S_x^{(i-1)}}{S_x^{(i-1)}} \times 100 \right| \quad (3)$$

where $S_x^{(i)}$ is the average strain in the x-direction at the end of the i^{th} iteration, it is given by

$$S_x^{(i)} = \frac{\sum_{e=1}^N S_x^{e(i)} V_e}{\sum_{e=1}^N V_e} \quad (4)$$

Here, $S_x^{(i)}$ is the average strain of an element e with volume V_e at the end of the i^{th} iteration. Also, N is total number of element in the FE model.

Using ANSYS APDL, the results presented in Table 4 correspond to the values of the average micro-generated strain and the subsequent error at each iteration of the proposed algorithm for various cross-sections of IDEs. As a result, three iterations are needed to obtain the new polarization distribution in the RVE within 1% error of the generated strain.

The developed poling process simulation was implemented in ANSYS APDL in order to calculate the electric field and the generated micro-strain in the longitudinal axis for the whole RVE. The different steps are summarized in Fig. 4.

3. Performance analysis for different RVEs dimensions

3.1 Electrical field distribution analysis and model validation

In this section, the authors use CFEM to investigate the electric field distribution within the proposed RVEs. Results of the electric field inside different RVEs are presented in Fig. 5. It is shown that the electric field distributions in different RVEs are inhomogeneous and anisotropic, three different regions can be identified:

- A region known as the Active Zone, characterized

by homogeneous and longitudinal electric field, between two constitutive IDEs.

- A region characterized by high electrical field concentration, underneath the electrodes, which paves the way to electric failure inside the material.
- A region known as the Dead Zone, characterized by transversal electric field underneath the electrodes. Its contribution to strain generation is very small.

Consequently, the generated strain along the longitudinal x-axis is highly inhomogeneous following the above observed variation of the electric field within the RVE. These observations are confirmed by Fig. 6, where contour plots of the strain distribution are presented. In fact, large variations of the strain are observed for all RVEs denoting large variations of the electric field underneath the electrodes.

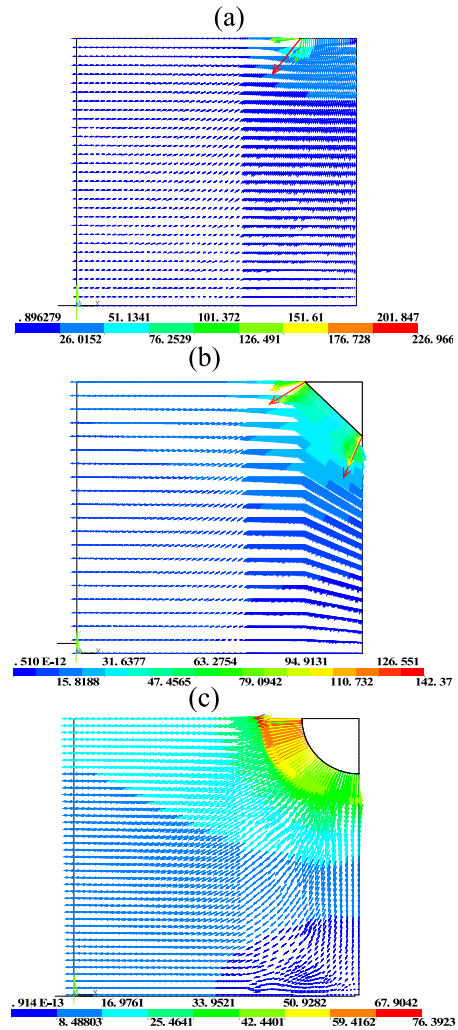


Fig. 5 Vector plots of electric field distribution for different RVEs

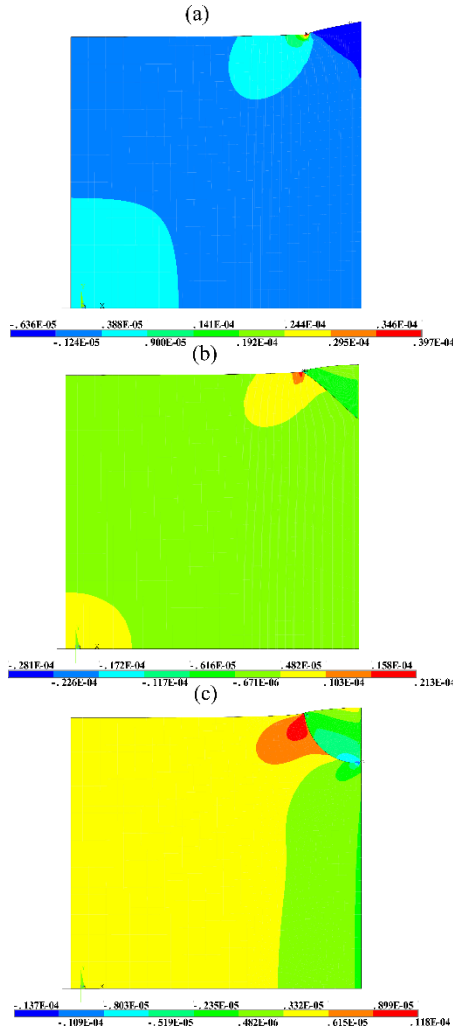


Fig. 6 Contour plots of the strain distribution in the x -direction for different RVEs

Table 5 Comparison between our numerical results for the electric field in the x -direction for classical electrodes and those obtained by Bowen *et al.* (2006) ($d/2 = 500\mu\text{m}$, $V = 250\text{V}$, $h_p/2 = 100\mu\text{m}$)

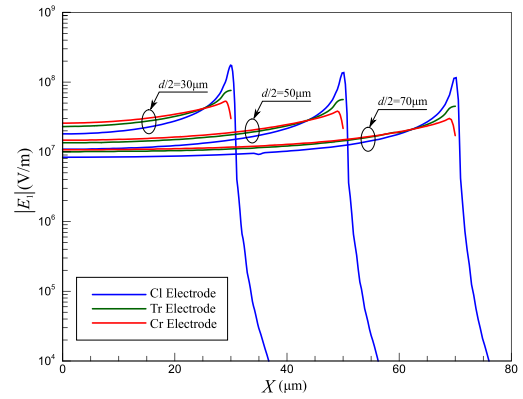
$b_e/2(\mu\text{m})$	Our results (CFEM) ($10^6\text{V}/\text{m}$)	Bowen <i>et al.</i> (2006) ($10^6\text{V}/\text{m}$)
200.0	0.460	0.457
50.0	0.447	0.444
12.5	0.400	0.397

The presented results can be validated with those published by Bowen *et al.* (2006), whose numerical analysis is based on CFEM and was only applied for classical configuration of IDEs. In Table 5, a comparison is presented between our results and those found in Bowen *et al.* (2006) concerning the electric field value in the x -direction between two consecutive electrodes (i.e., in the Active Zone), when different electrode's width are used. Very good

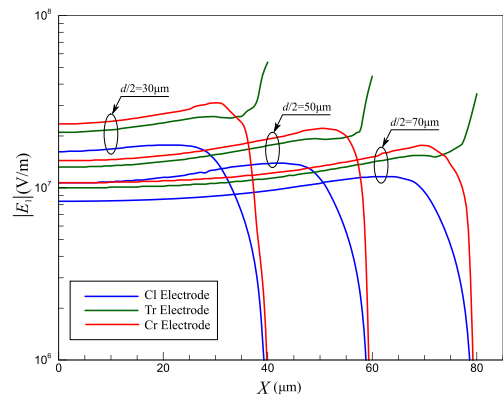
agreement is found between our results using CFEM and those found in Bowen *et al.* (2006).

3.2 Electric behavior for different IDE designs

Next, a comparative study between various IDE designs is proposed to show their influence on the electric field distribution. The numerical results, obtained by CFEM, are shown in Figs. 7. In Figs. 7(a) and 7(b), the electric field in the poling x -direction E_1 at the top surface (Boundary number 4, $y = h_p/2$) and $y = 3h_p/8$ for different configurations of IDEs: Classical (Cl), Triangular (Tr) and Circular (Cr). As can be seen in these Figs., the electric field intensity in the x -direction is lower for Cl configuration, except near to electrode edge at $y = h_p/2$ where a distinct peak is observed. This behavior can directly be interpreted as an increase of the actuator performance, when Cr and Tr designs are used, since IDEs are generally related to the d_{33} mode directly linked to E_1 . It is also expected that these Cr and Tr design allows a better reliability of the actuator because no excessive electric field is observed near electrodes. Moreover, when $y = 3h_p/8$, the longitudinal electric field intensity underneath the electrode is higher when the Tr configuration is used, and lower for the Cl one, as can be seen from Fig. 7(b).



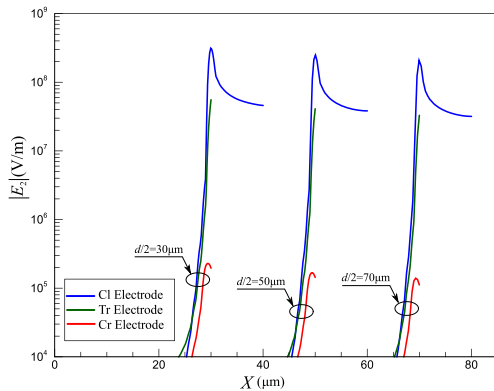
(a) Variation of $|E_1|$ along the x -direction at $y = h_p/2$



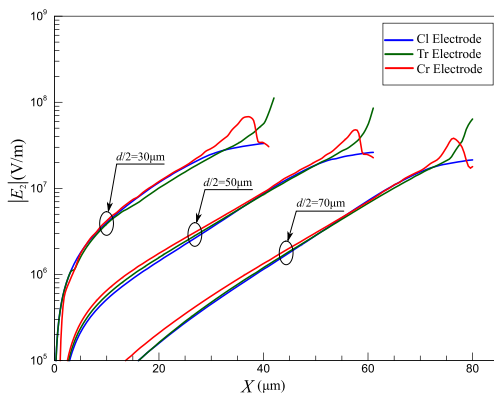
(b) Variation of $|E_1|$ along the x -direction at $y = 3h_p/8$

Fig. 7 FE results showing the effect of IDE cross-section design on the electric fields in the x -direction of the RVEs ($h_p/2 = 40\mu\text{m}$ and $b_e/2 = a = 10\mu\text{m}$)

Also, an analysis is suggested concerning the influence of the electrode configuration on the electric field in the thickness direction (i.e., y -direction). To this end, curves showing the variation of $|E_2|$ within RVEs with various electrode configurations, are plotted in Figs. 8(a) and 8(b). These Figs. show the electric field distribution along the y -direction at the substrate top surface (i.e., $y = h_p / 2$) and $y = 3h_p / 8$ for Cl, Tr and Cr configurations. As can be seen from Fig. 8(a), the electric field along the y -direction between two consecutive IDEs I almost canceled, for all electrode configuration, especially when $y = h_p / 2$. At the edge of the electrode, an intensification of the transversal electric field is captured, particularly when the Cl and Tr configurations are used. More importantly, when $y = 3h_p / 8$, the authors can note that the transversal electric field in the active zone is relatively insensitive to the variation of the cross-section of the electrode. In the Fig. 8(b), E_2 underneath the electrode is more important than its value between electrodes. This is more distinguishable when novel IDE configurations are adopted. Since this increase of the transversal electric field is located in the dead Zone, the performance of the system is not expected to be improved.



(a) Variation of $|E_2|$ along the x -direction at $y = h_p / 2$



(b) Variation of $|E_2|$ along the x -direction at $y = 3h_p / 8$

Fig. 8 FE results showing the effect of IDE cross-section design on the electric fields in the y -direction of the RVEs ($h_p / 2 = 40 \mu\text{m}$ and $b_e / 2 = a = 10 \mu\text{m}$)

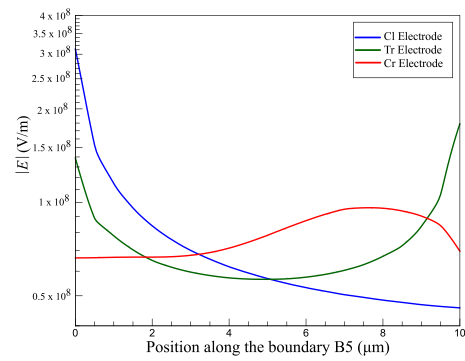


Fig. 9 FE results showing the variation of $|E|$ at the boundary B5 underneath the electrodes for different RVEs ($d / 2 = 40 \mu\text{m}$ and $h_p / 2 = 40 \mu\text{m}$)

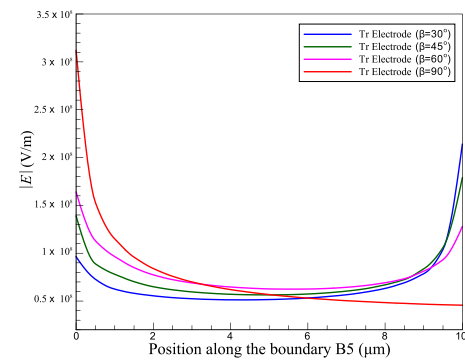


Fig. 10 FE results showing the variation of $|E|$ at the boundary B5 underneath electrode for triangular electrodes ($d / 2 = 40 \mu\text{m}$ and $h_p / 2 = 40 \mu\text{m}$)

In order to provide a better understanding of the electric field underneath electrode, it is observed that the total magnitude of the electric field $|E|$, for three cases of configurations. In this analysis, the length of the electrode (i.e., boundary B5) is kept equal to $10 \mu\text{m}$ for three cases of configurations, i.e., for Cl configuration; $b_e / 2 = 10 \mu\text{m}$, for Tr configuration; $b_e / 2 = 10 / \Pi \mu\text{m}$ and, for Cr configuration; $b_e / 2 = 10 / \Pi \mu\text{m}$. The results are given in Fig. 9, where the Cl configuration provides the highest intensification of the electric field near the electrode's edge. Similarly, the Tr configuration delivers an inhomogeneous and highly electric field distribution. In contrast, the Cr configuration offers a quasi-homogeneous and low electric field. As a consequence, the risk of premature failure may be expected to decrease significantly for the case of Cr configuration thanks of the low local electric field concentration.

Before closing this section, an investigation of the influence of the shape of the electrode is proposed, when a Tr configuration is used. In Fig. 10, we present the effect of the geometric parameter $\beta = \text{Arctg}(b_e / 2a)$ on $|E|$ underneath electrode. In this figure, β was the only

parameter that is varied, while the spacing between two consecutive IDEs, PZT thickness and the length of the electrode (i.e., boundary B_5) remained constant. Here, the authors remind that the case corresponding to $\beta = 90^\circ$ correspond to the Cl configuration. Since for high value of β , the electric field underneath the electrode shows global maximum peak. For values of β within 90° , the electric field is characterized by two maxima points on the left and the right sides of the electrode. As a result, the presence of geometric singularity in the case of Tr configuration increases the electric field concentration at the edge of the electrode. Also, one can notice here that the electric field concentration underneath the electrode locally changes with the variation of β . Indeed, the peak presenting the concentration of the electric field moves from left to right side of the electrode as β is decreased. As a result, for medium values of ($\beta = 45^\circ$ and $\beta = 60^\circ$), a relatively low electric field, under the electrode, is observed. It is clear that this reduction cuts down the risk of premature failure of the device due to electric breakdown.

4. Parametric analysis

Simply using the CFEM and neglected the influence of the poling process and the resulting inhomogeneous poling state of the PZT material, gives little insight into the effects of the cross-section of the electrode on the strain and electric field distributions inside the RVE. To increase precision of the FEM model, it is desirable to introduce the local effects resulting from highly inhomogeneous electric field state of the PZT material. These local effects have been found to have small influence in some cases (Deraemaeker and Nasser 2010). However, these effects can be useful for a better understanding of the behavior of such devices and a more accurate prediction of their capabilities and performances. In the following sections, it is proven, through a detailed parametric analysis, that the use of the AFEM can be very useful for studying influence of the electrode's geometry of the device.

4.1 Effect of the electrode separation

One of the important parameter to be examined is the electrode separation d . Here, it is varied while both electrode width and piezoelectric material thickness remained constant ($b_e / 2 = 10 / \Pi \mu m$ and $b_p / 2 = 10 / \Pi \mu m$). Numerical results summarizing the effect of electrode separation are presented in Fig. 11(a). The plots show large discrepancies between values obtained from CFEM and AFEM. It is clear that the AFEM should be adopted for performance analysis especially for low electrode separation. One can note in Fig. 11(a) that devices using IDEs with Cr configuration can generate more strain, especially for low values of electrode separation. To quantify this fact, approximately 150% of the maximum strain increase can be achieved with Cr configuration, compared to the Cl one.

We define the coefficient α that characterizes the electric field orientation in the x direction using the following relation

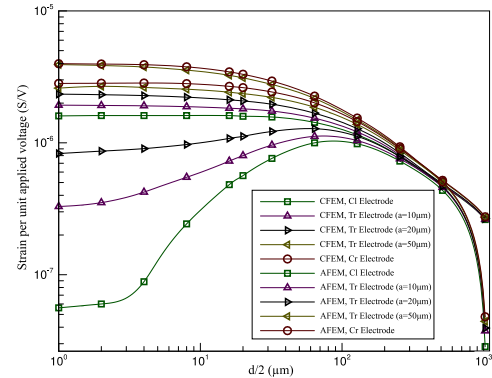
$$\alpha = \frac{|\bar{E}_1|}{|\bar{E}_1| + |\bar{E}_2|}$$

where \bar{E}_1 and \bar{E}_2 are the mean values of the electric field in the x and y -directions, respectively, given by

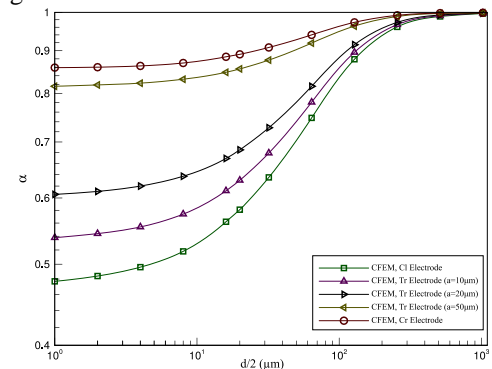
$$\bar{E}_i = \frac{\sum_{e=1}^N E_i^e V_e}{\sum_{e=1}^N V_e}, \quad i=1,2$$

where \bar{E}_i , $i = \{1,2\}$ is, respectively, the average electric field in the x and y directions of an element e with volume V_e , at the end of the simulation.

Fig. 11(b) presents the variation of the coefficient α with respect to the electrode separation d for different configurations of electrodes using the CFEM. As can be seen from this figure, the RVE using IDEs with Cr configuration provides the optimum value of α , corresponding to high strength of electric field in the x -direction, thus the mode d_{33} is expected to be further activated.



(a) Variation of the strain per unit applied voltage with $d/2$ by using CFEM and AFEM



(b) Variation of the coefficient α with $d/2$ by using the CFEM

Fig. 11 The effect of the electrode separation $d/2$ on the performance of The RVE ($b_e / 2 = 50 \mu m$ and $h_p / 2 = 100 \mu m$)

Table 6 Effect of the variation of electrode separation on material's polarization ($h_p/2=100\mu\text{m}$, $a=20\mu\text{m}$ and $b_e/2=50\mu\text{m}$), UP: unpoled, P: fully poled

IDEs Design		$d/2(\mu\text{m})$						
Cl design	UP Material	0.50	0.41	0.13	0.16	0.41	2.5	13.55
	P Material	98.23	98.75	99.34	99.08	98	89.94	0.55
Tr design	UP Material	0.28	0.19	0.13	0.34	0.16	2.94	14.94
	P Material	97.87	98.47	99.07	98.38	98.63	83.52	0.20
Cr design	UP Material	0.19	0.01	0.01	0.31	0.42	2.57	10.35
	P Material	99.32	99.60	99.52	98.83	97.72	87.12	0

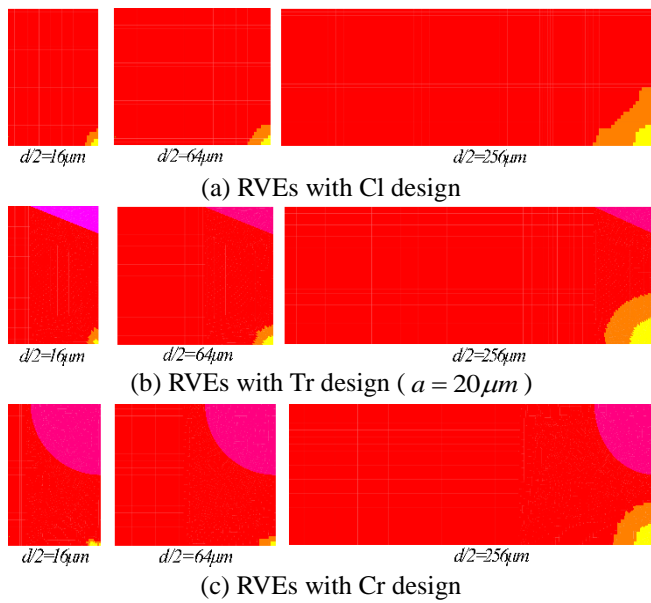


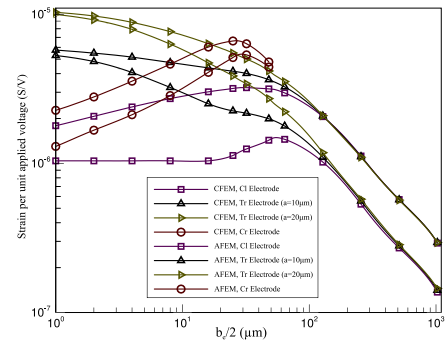
Fig. 12 Polarization distribution with different values of d for various cross-sections of electrode ($b_e/2=50\mu\text{m}$ and $h_p/2=100\mu\text{m}$). Red color indicates poled material, orange color indicates partially-poled material and yellow indicates unpoled material

Considering the same figure, α is insensitive to the variation of the electrode separation if this latter is higher than $10^3\mu\text{m}$. That's why a matching between curves of the micro-strain's average is detected for high values of electrode separation, as shown in Fig. 11(a).

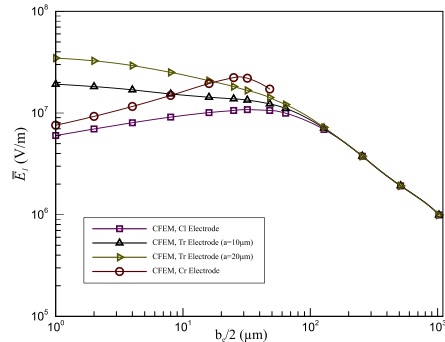
Moreover, it is worthwhile to note that the behavior of the average of the micro-strain, when electrode separation is varied, is monotonic, when using CFEM i.e. local details are neglected. In contrast, this behavior becomes non monotonic, when the local variation of the polarization and the material properties are considered in the AFEM. More importantly, a significant mismatch between FE results obtained from CFEM and AFEM can be observed in Fig. 11-a can be explained as follows:

- As the electrode separation becomes higher, the strength of electric field decreases allowing a reduction of the proportion of the poled piezoelectric material. As a result, the generated strain is expected to be reduced, when the local effects are considered. The proportion of the poled and unpoled piezoelectric materials of RVEs using IDEs with various designs for different values of electrode separation are summarized in Table 6. In addition, to confirm the effect of the local details, Fig. 12 shows the polarization distribution within RVEs for various values of electrode separation. The simulated poling resulted in the material distribution given in Figs. 12, clearly indicating the poled, partially-poled and unpoled piezoelectric material by red, orange and yellow, respectively.

- As the electrode separation becomes lower, the piezoelectric material turn out to be fully poled in the thickness direction. However, the proportion of dead zone becomes higher allowing a drop of the generated strain in the longitudinal direction, when the local effects are accounted.



(a) Variation of the strain per unit applied voltage with $b_e/2$ by using CFEM and AFEM



(b) Variation of the coefficient \bar{E}_1 with $b_e/2$ by using the CFEM

Fig. 13 The effect of the electrode separation $b_e/2$ on the performance of The RVE ($h_p/2=50\mu\text{m}$ and $d/2=10\mu\text{m}$)

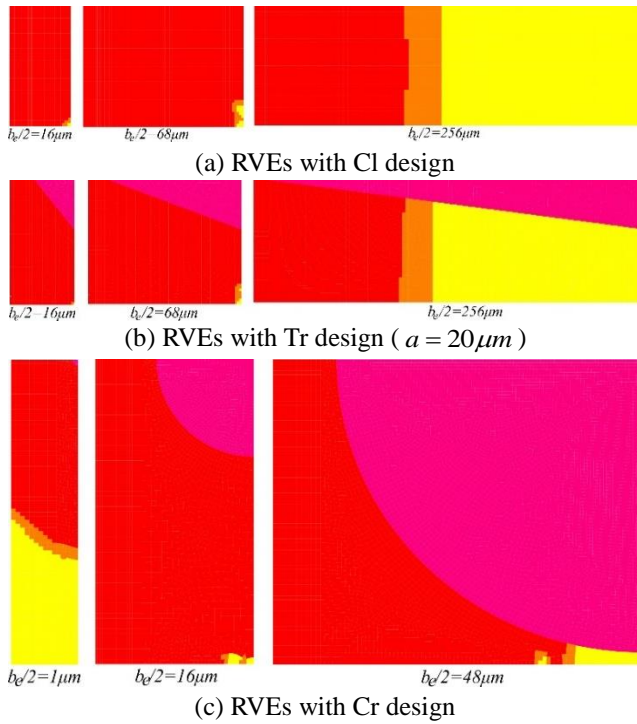


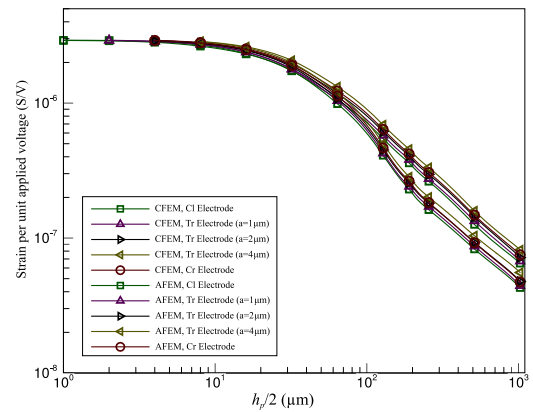
Fig. 14 Material distribution in the 2D FEM of RVEs with different values of the electrode width for RVEs with various cross-sections of electrodes ($h_p/2 = 50\mu\text{m}$ and $d/2 = 10\mu\text{m}$). Red color indicates poled material, orange color indicates partially-poled material and yellow indicates unpoled material

4.2 Effect of the electrode width

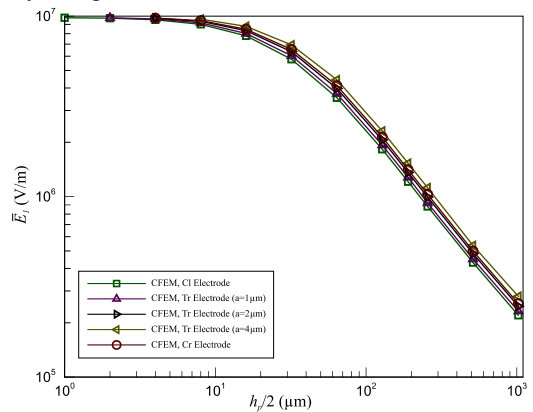
Here, the analysis of the effect of the electrode width b_e on the micro-strain average per unit applied voltage of the RVEs using different configurations of IDEs, is proposed.

In fact, numerical results summarizing the effect of electrode width are presented in Fig. 13(a). In this analysis, the electrode width was varied, while the electrode separation and piezoelectric material thickness remained constant ($h_p/2 = 50\mu\text{m}$ and $d/2 = 10\mu\text{m}$).

By neglecting the local effects (CFEM), non-monotonic behavior of the strain with respect to electrode width is observed, when the Cl configuration is used. The optimum occurs approximately at $b_e/h_p = 0.5$. This result is in line with that obtained in Bowen *et al.* (Bowen *et al.* 2006). Similarly to the Cl configuration, the behavior of the strain is clearly nonmonotonic, when the cross-section of electrode is Cr. Its optimum occurs approximately at the same ratio $b_e/h_p = 0.5$. In contrast, the behavior becomes monotonic when the cross-section of electrode changes to Tr. As can be seen from Fig. 13(a), the average of the strain per unit applied voltage decreases monotonically by increasing electrode width. More importantly, the generated strain is insensitive to the variation of the cross-section of electrode when large values of the electrode width are used.



(a) Variation of the strain per unit applied voltage with $b_e/2$ by using CFEM and AFEM



(b) Variation of the coefficient \bar{E}_1 with $b_e/2$ by using the CFEM

Fig. 15 The effect of the electrode separation $b_e/2$ on the performance of The RVE ($h_p/2 = 50\mu\text{m}$ and $d/2 = 10\mu\text{m}$)

Another interesting point to mention in Fig. 13(a) is intersections between curves for novel IDEs designs. For low values of $b_e/2$, the strain is higher in the case of Tr design. For the values of electrode width $b_e/2$ higher than the value of a , the strain becomes higher in the case of Cr design. To understand the origin of this behavior, it is necessary to examine how the electric field in the piezoelectric material is affected by the electrode width at constant thickness and separation ($h_p/2 = 50\mu\text{m}$ and $d/2 = 10\mu\text{m}$). Fig. 13(b) shows the average of the electric field in the longitudinal direction as a function of electrode width. In fact, the behavior of the generated strain with the electrode width follows precisely the variation of the electric field in the longitudinal direction within the RVEs for all IDEs designs.

By accounting for the local behavior of the piezoelectric material in the AFEM, one can note a clear discrepancy between curves calculated using CFEM and AFEM. The reason behind this discrepancy can be seen by examining Table 7, where the polarization state of the piezoelectric material is calculated for various values of electrode width.

Table 7 Effect of the variation of the electrode width on state of material's polarization ($h_p/2 = 50\mu m, a = 20\mu m$ and $d/2 = 10\mu m$)

IDEs Design		$b_e/2(\mu m)$							
CI design	UP Material	35	14.25	0	0.31	4.92	58.61	67.69	
	P Material	56.91	74	99.40	98.92	79.54	36.92	30.76	
Tr design	UP Material	0.81	0.01	0	0.12	7.65	45.30	55.99	
	P Material	98.81	99.94	99.93	99.62	78.52	52.28	42.63	
Cr design	UP Material	31.44	6.53	0	-	-	-	-	
	P Material	59.61	86.58	99.92	-	-	-	-	

Also, contour plots of the polarization state are presented in Fig. 14, for different values of the electrode width.

One can conclude that for small electrode width for Cr and CI designs, the percentage of unpoled piezoelectric material is higher when $b_e/2$ is reduced, thus the generated strain diminishes. As the electrode width becomes larger, the piezoelectric material is poled in the thickness direction, thus the strain in the longitudinal direction is reduced (Fig. 13(a)). Also, with large electrode width, the percentage of unpoled piezoelectric material becomes higher as $b_e/2$ is increased (Table 7). As a result, the generated strain decreases (Fig. 13).

4.3 Effect of the PZT thickness

The thickness of the piezoelectric material is also worth investigating. The effect of this thickness represented by the parameter $h_p/2$ is analyzed in Figs. 15, where the average strain per unit applied voltage and generated electrical field in the longitudinal direction are calculated.

The piezoelectric material thickness $h_p/2$ is varied, while the electrode separation and electrode width remained constant ($b_e/2 = 2\mu m$ and $d/2 = 100\mu m$). As can be shown from Fig. 15(a), when $h_p/2$ increases, the generated strain decreases. According to the same figure, it is clear that the RVE with Tr configuration generates more strain, especially when $a = 4\mu m$ and for high values of PZT thickness. In the other hand, the same strain is observed for different IDEs designs for very low values of PZT thickness.

In order to get more insight into the behavior observed in Fig. 15(a), the authors analyse the effect of the PZT thickness on the mean value of the electric field in the longitudinal direction. Fig. 15(b) shows the variation of the $|\bar{E}_1|$ with the PZT thickness. It demonstrates that the variation of $|\bar{E}_1|$ follows a similar behavior than the generated strain.

Table 8 Effect of the variation of PZT thickness on the state of material's polarization ($d/2 = 100\mu m, a = 2\mu m$ and $b_e/2 = 2\mu m$)

IDEs Design		$h_p/2(\mu m)$							
CI design	UP Material	0	0	0.15	0.75	4.5	70	83.83	
	P Material	100	100	99.53	96.37	77.87	18.94	10.19	
Tr design	UP Material	-	0	0.15	0.16	3.71	68.87	83.35	
	P Material	-	99.81	99.07	98.38	81.44	20.34	10.54	
Cr design	UP Material	-	0	0	0.55	4.38	65.75	82.13	
	P Material	-	100	99.78	97.09	83.99	23.18	13.26	

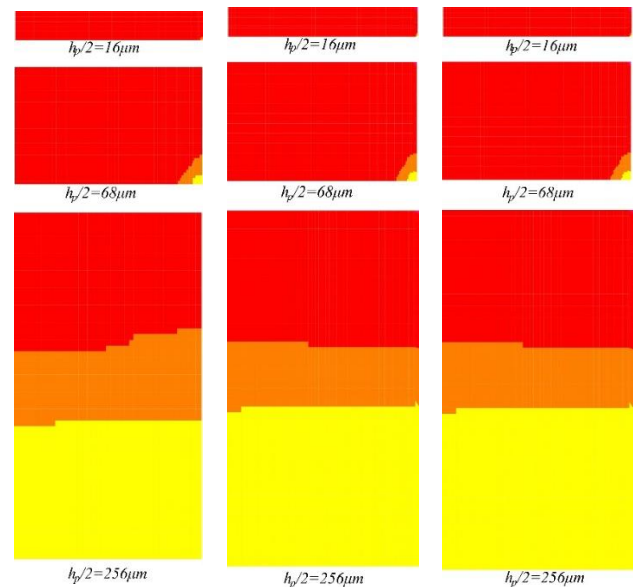


Fig. 16 Material distribution in the 2D FEM of RVEs with different values of the electrode width for RVEs with various cross-sections of electrodes ($b_e/2 = a = 2\mu m$ and $d/2 = 100\mu m$)

Furthermore, by considering the local effects in the AFEM, one can note a reduction of the generated strain, especially for high values of PZT thickness. This can be explained by the fact that, when the PZT thickness is increased, the strength of electric field within the RVE diminished allowing the reduction of the portion of poled piezoelectric material.

5. Conclusions

Novel designs of d_{33} mode piezoelectric microstructures are proposed in this work. It has been proven that the new geometry of the electrodes, increase the performances of microscale actuators, sensors as well as energy harvesters. A numerical parametric analysis of different designs for

piezoelectric structures has been carried out on a representative volume element for classical, triangular and circular cross-sections electrodes. Modeling of the piezoelectric structure has given an insight into how the strain response is affected by electrode shape, width, substrate thickness and electrode separation. Advanced numerical FE models, which take into account the presence of the electrode and local polarization due to high variation of the electric field, has been developed. Also, classical numerical models, in which the PZT material is fully poled in the longitudinal direction, were used for a comparative study. Numerical results show that the novel electrode designs (circular and triangular electrodes) can significantly ameliorate the micro-strain by selecting the appropriate geometrical parameters. Approximately 150% increase of the generated strain can be achieved with circular configuration, compared to the classical one. In addition, the obtained numerical results demonstrate that the electrical field concentrations, in case of novel electrode designs, can be significantly decreased, allowing reduction of premature electrical breakdown.

References

- Alghisi, D., Dalola, S., Ferrari, M. and Ferrari, V. (2015), "Triaxial ball-impact piezoelectric converter for autonomous sensors exploiting energy harvesting from vibrations and human motion", *Sensors. Actuat. A: Phys.*, **233**, 569-581.
- Ammar, Y., Buhrig, A., Marzencki, M., Charlot, B., Basrour, S., Matou, K. and Renaudin, M. (2005), "Wireless sensor network node with asynchronous architecture and vibration harvesting micro power generator", *Proceedings of the 2005 Joint Conf. on Smart Objects and Ambient intelligence: Innovative Context-Aware Services: Usages and Technologies*, Grenoble, France.
- Avsar, A.L. and Sahin, M. (2016), "Bimorph piezoelectric energy harvester structurally integrated on a trapezoidal plate", *Smart Struct. Syst.*, **18**(2), 249-265.
- Beckert, W. and Kreher, W.S. (2003), "Modelling Piezoelectric modules with Interdigitated electrode structures", *Comput. Mater. Sci.*, **26**, 36-45.
- Bowen, C.R., Bowles, A., Drake, S., Johnson, N. and Mahon, S. (1999), "Fabrication and finite element modelling of interdigitated electrodes", *Ferroelectrics*, **228**, 257-269.
- Bowen, C.R., Nelson, L.J., Stevens, R., Gain, M.G. and Stewart, M. (2006), "Optimization of Interdigitated electrodes for piezoelectric actuators and Active Fiber composites", *J. Electroceram.*, **16**, 263-269.
- Deraemaeker, A. and Nasser, H. (2010), "Numerical evaluation of the equivalent properties of Macro Fiber Composite (MFC) transducers using periodic homogenization", *Int. J. Solids Struct.*, **47**, 3272-3285.
- Ghodssi R. and P. Lin (2011), *MEMS Materials and Processes Handbook*, USA.
- Hagood, N.W., Kindel, R., Ghandi, K. and Gaudenzi, P. (1993), "Improving transverse actuation of piezoceramics using interdigitated surface electrodes", *Proceedings of the SPIE 1917, Smart Structures and Materials 1993: Smart Structures and Intelligent Systems*, 341, Albuquerque, NM, USA, February, 1.
- Hong, Y.K., Moon, K.S., Levy, M. and Vanga, R.R. (2006), "Single-crystal film piezoelectric sensors, actuators and energy harvesters with interdigitated electrodes", *Ferroelectrics*, **342**, 1-13.
- Inman, D.J., Ahmadian, M. and Claus, R.O. (2001), "Simultaneous active damping and health monitoring of aircraft panels", *J. Intel. Mat. Syst. Str.*, **12**, 775-783.
- Isarakorn, D., Briand, D., Janphuang, P., Sambri, A., Gariglio, S., Triscone, J.M., Guy, F., Reiner, J.W., Ahn, C.H. and Rooij, N.F. (2011), "The realization and performance of vibration harvesting MEMS devices based on an epitaxial piezoelectric thin film", *Smart Mater. Struct.*, **20**, 025015.
- Jamal, G.A., Rahman, S.L., Rana, M.M., Nafis, S.A.S., Huda, M.M. and Rahman, S.N. (2015), "An alternative approach to wind power generation using piezoelectric material", *Am. J. Renew. Sust. Energ.*, **1**, 45-50.
- Jemai, A., Najar, F., Chafra, M. and Ounaies, Z. (2014), "Mathematical modeling of an active-fiber composite energy harvester with interdigitated electrodes", *J. Shock Vib.*, 2014.
- Jemai, A., Najar, F., Chafra, M. and Ounaies, Z. (2016), "Modeling and parametric analysis of a unimorph piezocomposite energy harvester with interdigitated electrodes", *Compos. Struct.*, **135**, 176-190.
- Kim, S.B., Park, H., Kim, S.H., Wickle, H.C., Park, J.H. and Kim, D.J. (2013), "Comparison of MEMS PZT cantilevers based on d31 and d33 modes for vibration energy harvesting", *J. Microelectromech. Syst.*, **22**, 26-33.
- Lee, B.S., Lin, S.C., Wu, W.J., Wang, X.Y., Chan, P.Z. and Lee, C.K. (2009), "Piezoelectric MEMS generators fabricated with an aerosol deposition PZT thin film", *J. Micromech. Microeng.*, **19**, 065014.
- Li, Y.X., Zhang, S.Q., Schmidt, R. and Qin, X.S. (2016), "Homogenization of macro-fiber composite using Reissner-Mindlin plate theory", *J. Intel. Mat. Syst. Str.*, **27**, 2477-2488.
- Lu, F., Lee, H.P. and Lim, S.P. (2004), "Modeling and analysis of micro piezoelectric power generators for micro-electromechanical-systems applications", *Smart Mater. Struct.*, **13**, 57-63.
- Moore, S.I. and Yong, Y.K. (2017), "Design and characterisation of cantilevers for multi-frequency atomic force microscopy", *IET Micro & Nano Lett.*, **12**, 315-320.
- Murali, P. (2008), "Recent progress in materials issues for piezoelectric MEMS", *J. Am. Ceram. Soc.*, **91**, 1385-1396.
- Nguyen, N.T., Yoon, B.S., Park, K.H. and Yoon, K.J. (2011), "Analytical model and optimal design of a d33-mode active layer for the lightweight unimorph piezo-composite actuator", *J. Electroceram.*, **26**, 175-184.
- Paradies, R. and Melnykowycz, M.M. (2010), "State of stress in piezoelectric elements with interdigitated electrodes", *J. Electroceram.*, **24**, 137-144.
- Paradies, R., Hertwig, M. and Elspass, W.J. (1996), "Shape control of an adaptive mirror at different angles of inclination", *J. Intel. Mat. Syst. Str.*, **7**, 203-210.
- Prakash, S., Kumar, T.R., Raja, S., Dwarakanathan, D., Subramani, H. and Karthikeyan, C. (2016), "Active vibration control of a full scale aircraft wing using a reconfigurable controller", *J. Sound Vib.*, **361**, 32-49.
- Sahu, K.C., Tuhkuri, J. and Reddy, J.N. (2015), "Active structural acoustic control of a softcore sandwich panel using multiple piezoelectric actuators and Reddy's higher order theory", *J. Low Frequency Noise, Vibration and Active Control*, **34**, 385-411.
- Shen, D., Park, J.H., Ajitsaria, H., Choe, S.Y., Wickle, H.C. and Kim, D.J. (2008), "The design, fabrication and evaluation of a MEMS PZT cantilever with an integrated Si proof mass for vibration energy harvesting", *J. Micromech. Microeng.*, **18**, 055017.
- Sodano, H.A., Lloyd, J. and Inman, D.J. (2006), "An experimental comparison between several active composite actuators for power generation", *Smart Mater. Struct.*, **15**, 1211-1216.
- Tadigadapa S. and Mateti, K. (2009), "Piezoelectric MEMS

- sensors: state-of-the-art and perspectives”, *Meas. Sci. Technol.*, **20**, 092001.
- Trindade, M.A. and Benjeddou, A. (2011), “Finite element homogenization technique for the characterization of d15 shear piezoelectric macro-fibre composites”, *Smart Mater. Struct.*, **20**(7), 075012.
- Zhang, S.Q., Chen, M., Zhao, G.Z., Wang, Z.X., Schmidt, R. and Qin, X.S. (2017), “Modeling techniques for active shape and vibration control of macro-fiber composite laminated structures”, *Smart Struct. Syst.*, **19**(6), 633-641.
- Zhang, S.Q., Li, Y.X. and Schmidt, R. (2015), “Modeling and simulation of macro-fiber composite layered smart structures”, *Compos. Struct.*, **126**, 89-100.
- Zhang, S.Q., Wang, Z.X., Qin, X.S., Zhao, G.Z. and Schmidt, R. (2016), “Geometrically nonlinear analysis of composite laminated structures with multiple macro-fiber composite (MFC) actuators”, *Compos. Struct.*, **150**, 62-72.

HJ